



Polarization-Enhanced direct Z-scheme ZnO-WO_{3-x} nanorod arrays for efficient piezoelectric-photoelectrochemical Water splitting

Ying Chen^{a,b,1}, Li Wang^{a,b,1}, Ruijie Gao^{a,b,1}, Yong-Chao Zhang^{a,b}, Lun Pan^{a,b,*}, Chenyu Huang^{a,b}, Kan Liu^a, Xin-Yuan Chang^a, Xiangwen Zhang^{a,b}, Ji-Jun Zou^{a,b}

^a Key Laboratory for Green Chemical Technology of the Ministry of Education, School of Chemical Engineering and Technology, Tianjin University, Tianjin 300072, China

^b Collaborative Innovative Center of Chemical Science and Engineering (Tianjin), Tianjin 300072, China

ARTICLE INFO

Keywords:

Piezoelectric polarization
Photoelectrochemical water splitting
Direct Z-scheme heterojunctions
ZnO
WO_{3-x}

ABSTRACT

Photosynthesis with Z-scheme charge transfer has been recognized as an efficient pathway to achieve solar-energy conversion. Herein, the all-solid-state direct Z-scheme ZnO-WO_{3-x} nanorod arrays were synthesized by *in-situ* solvothermal treatment for highly piezoelectric (PE)-photoelectrochemical (PEC) water splitting. The chemical bonding between WO_{3-x} and ZnO via W-O-Zn and the inherent band structures/Fermi levels drive the formation of direct Z-scheme charge-transfer pathway. Importantly, the optimized structure (Zn-W-5) shows higher PEC activities with high photocurrent density of 2.39 mA/cm² at 1.23 V vs. RHE, which is 2.13 times higher than pure ZnO. Surprisingly, the obvious PE polarization of ZnO increases its Fermi level toward conduction band and significantly enhances Z-scheme effect between ZnO and WO_{3-x}. Especially, the best sample (Zn-W-5-1000 rpm) shows a photocurrent of 3.38 mA/cm² at 1.23 V vs. RHE, which is 3.02 times higher than pure ZnO. This work provides a facile PE polarization approach for enhancement of Z-scheme charge-transfer process.

1. Introduction

With increasing demands for alternative fuel sources, extensive research has focused on discovering ways to convert and utilize the renewable energy (like solar light) [1,2], and hydrogen production via photoelectrochemical (PEC) water splitting is one of the most promising routes [3]. Since TiO₂ was first reported as effective photoelectrode for PEC water splitting by Fujishima et al., growing attention has been paid to fabricate the efficient photoelectrodes [4–10]. Among them, n-type zinc oxide (hexagonal wurtzite ZnO) has emerged as a promising photoanode material, attributed to its high catalytic efficiency, low cost, environmental sustainability and piezoelectric properties [11–14]. However, the rapid charges recombination significantly limits the PEC performance of ZnO, with its photo-to-current conversion efficiency (η_{STH}) much lower than the theoretical one. To significantly improve the charge-separation efficiency, the construction of Z-scheme heterojunction has been regarded as a very promising approach [4,15–19], because this structure can simultaneously achieve efficient charge separation and maintain the high redox ability.

With the matched band structure and Fermi level of ZnO, tungsten oxide (WO₃) could be a good candidate to assemble Z-scheme

heterojunctions, with high carrier mobility and strong oxidation ability [20–22]. In this Z-scheme system, the photo-induced electrons on WO₃ with lower conduction band potential will combine with the holes on ZnO with higher valence band potential, and the electrons and holes with stronger redox ability remain on ZnO and WO₃, respectively. However, there are still no reports about the construction of direct Z-scheme ZnO-WO₃ heterojunctions.

Generally, the electron acceptor/donor (A/D) pair and metal conductors are common electron mediators to realize Z-scheme charge transfer [5,15,23], but it will cause the difficulty and complexity to the preparation. Alternatively, the direct Z-scheme system without conductors is more facile and cost-effective. Specially, the creation and modulation of oxygen defects in WO₃ crystal are facile [24–26], and the defects on the contact interface can form ohmic contact and lower the interfacial electric resistance [27], benefiting the formation of direct Z-scheme charge transfer.

Therefore, in this work, we coupled ZnO nanorod arrays with surface WO_{3-x} nanoparticles, by *in-situ* solvothermal method, to construct the highly effective direct Z-scheme photoanodes. Importantly, the optimized sample Zn-W-5 shows higher PEC activities with the photocurrent density as high as 2.39 mA/cm² at 1.23 V vs. RHE, which is 2.13

* Corresponding author.

E-mail address: panlun76@tju.edu.cn (L. Pan).

¹ The authors contributed to this article equally.

times higher than pure ZnO. More interestingly, the piezoelectric (PE) polarization in ZnO has been found to significantly modulate the Fermi level and further the interface band bending of ZnO-WO_{3-x}. Accordingly, the best sample (Zn-W-5 under 1000 rpm stirring) shows a very high photocurrent of 3.38 mA/cm² at 1.23 V vs. RHE, which is 3.02 times higher than pure ZnO.

2. Experimental methods

2.1. Materials

Zn(NO₃)₂ was obtained from Aladdin Chemicals. WCl₆ was obtained from J&K Chemical. Hexamethylenetetramine (HMT), acetone, methanol and ethanol were gained from Tianjin Yuanli Industrial Corporation. Milli-Q ultrapure water (> 18 mΩ·cm) was used in all experiments. All reagent used were analytical grade and used without further purification.

2.2. Preparation

2.2.1. ZnO nanorod arrays

ZnO seed layer: A FTO coated glass was cleaned with acetone, ethanol and water for 30 min in sequence. Then, ZnO seed layer was spin-coated on the FTO glass by aqueous solutions containing Zn(NO₃)₂ (0.1 M) and HMT (0.1 M). After that, the substrates were annealed at 300 °C for 10 min in air to stabilize ZnO seed layer.

ZnO nanorod arrays: 0.893 g Zn(NO₃)₂ and 0.423 g HMT were mixed in 30 mL deionized water under stirring for 30 min, then the mixed aqueous solutions were transferred into a 50 mL Teflon-lined autoclave with the above ZnO seed layer/FTO inserted, and then heated at 95 °C for 9 h, finally, the obtained ZnO nanorod arrays were washed by water and then dried at 60 °C for overnight (namely ZnO NA).

2.2.2. Decoration of WO₃ on ZnO NA

m mg (*m* = 1, 5, 10, 15) WCl₆ were dissolved into 30 mL methanol. After stirring for 30 min, the mixed solution was transferred into 50 mL Teflon-lined autoclave with the above ZnO NA/FTO glass inserted. Then the autoclave was sealed and heated at 180 °C for 3 h. Finally, the obtained samples were washed by ethanol for several times and annealed at 400 °C for 1 h with a heating rate of 5 °C/min (namely Zn-W-

m). The preparation procedure is shown in Fig. 1.

2.3. Characterizations

XRD patterns were conducted using Bruker AXS D8-Focus X-ray diffractometer equipped with Cu Kα radiation at 40 kV and 40 mA at scanning rate of 4°/min. SEM images were observed using a field emission scanning electron microscope (Hitachi, S-4800). High-resolution TEM observations were carried out with a Tecnai G² F-20 transmission electron microscope, and the energy dispersive spectrum (EDS) characterization was performed with an EDX system attached to TEM. X-ray photoelectron spectrum (XPS) was conducted with a PHI-1600 X-ray photoelectron spectroscope equipped with Al Kα radiation. Steady-state photoluminescence (PL) spectra were measured by a Horiba Jobin Yvon Fluorolog 3-21 with the excitation light at 325 nm. Time-resolved anisotropy decays and quantum yield were recorded on a FLS920 system (Edinburgh Instruments, BJ) utilizing time-correlated single photon count. UV-vis diffuse reflectance spectra (UV-vis DRS) were obtained from a Hitachi U-3100 spectrometer equipped with a 60 mm diameter integrating sphere using BaSO₄ as the reflectance sample.

2.4. Photocatalytic measurements

2.4.1. PEC measurements

PEC performances of Zn-W-*m* photoanodes were evaluated in a typical three-electrode quartz cell with Pt wire as counter electrode and saturated Ag/AgCl as a reference electrode, using CHI 660E electrochemical workstation. The electrolyte for PEC water splitting was 1 M Na₂SO₄ aqueous solution (pH = 7). The illumination source was a 300 W Xe arc lamp (100 mW·cm⁻², PLS-SXE300UV, Beijing Trusttech. Co. Ltd).

Linear sweep voltammetry (LSV) was monitored while sweeping the potential to the positive direction with a scan rate of 10 mV/s. The potential vs. Ag/AgCl reference electrode was converted to the potential vs. RHE according to the Nernst equation: $E \text{ (vs. RHE)} = E \text{ (vs. Ag/AgCl)} + 0.0591 \times \text{pH} + 0.197$ [28,29]. Electrochemical impedance spectra (EIS) measurements were carried out with a sinusoidal ac perturbation of 10 mV applied over the frequency range of 1-10⁵ Hz.

Incident photon to current conversion efficiency (IPCE) was measured using a Zolix Solar Cell quantum efficiency (QE)/IPCE

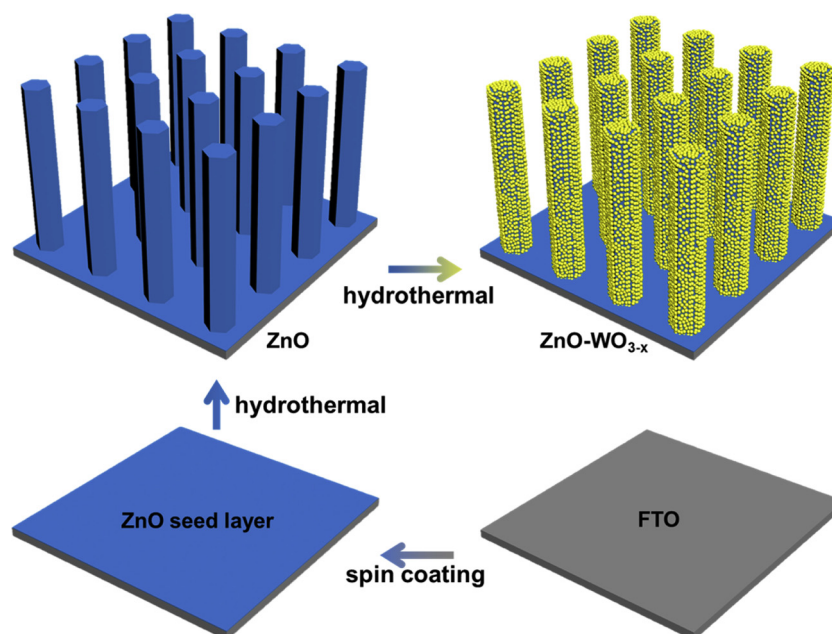


Fig. 1. Schematic illustration of Zn-W-*m* nanorods synthesized via the solvothermal method.

measurement system (Zolix Solar Cell Scan 100) with a 150 W Xe lamp equipped with a monochromator (Omni- λ 3007). A standard silicon photodiode (SI 200-STD) was used to calibrate the incident light intensity. IPCE spectra was measured at the wavelength from 300 nm to 450 nm at a potential of 0.5 V vs. Ag/AgCl. The IPCE value was calculated according to Eq. 1 [30]:

$$\text{IPCE}(\lambda) = \frac{1240 \times J(\lambda)}{\lambda \times P(\lambda)} \times 100\% \quad (1)$$

where λ is the wavelength (nm), $J(\lambda)$ is the photocurrent density ($\text{mA}\cdot\text{cm}^{-2}$), and $P(\lambda)$ is the incident power density of the monochromatic light ($\text{mW}\cdot\text{cm}^{-2}$).

The applied-bias power efficiency (ABPE) for a water-splitting photoelectrode that requires an applied voltage can be evaluated using Eq. 2 [31]:

$$\text{ABPE} = \frac{I \times (1.23 - V_{\text{app}})}{P_{\text{light}}} \times 100\% \quad (2)$$

where V_{app} is the applied voltage vs. RHE, I is the measured current density, and P_{light} is the power density of the illumination.

2.4.2. PEC H_2 and O_2 evolution measurements

Using Ar as a carrier gas, H_2 and O_2 gases evolved from the PEC cell were analyzed using a gas chromatograph (450-GC, 5 A molecular sieve column) equipped with a thermal conductivity detector (TCD). The light source and electrolyte were the same as those used for the above PEC measurements, and the gas products were sampled at each 10 min.

2.4.3. PE-PEC measurements

Piezoelectric-photoelectrochemical (PE-PEC) was measured with the above PEC system by adding stirring apparatus (magnetic stir of the solution in the test cell) as the trigger for piezoelectric effect. Linear Sweep Voltammetry (LSV) was measured at the scan rate of 10 mV/s.

2.4.4. Photodeposition of PbO_2

Charge-transfer pathways were examined by *in-situ* photodeposition of PbO_2 [16,17,32]. 200 mg $\text{Pb}(\text{NO}_3)_2$ was dispersed into 60 mL water with magnetic stirring for 30 min. Then the tested sample was placed into the solution, which was then irradiated with a 500 W Xe arc lamp ($100 \text{ mW}\cdot\text{cm}^{-2}$, PLS-SXE500UV, Beijing Trusttech. Co. Ltd) for 1 h. Finally, the obtained sample was washed and dried at room temperature for further characterization.

2.5. Density functional theory (DFT) calculations

Density functional theory (DFT) calculations were performed to confirm the Fermi levels of the two semiconductors. All density functional theory calculations were carried out with the Vienna Ab-initio Package (VASP) [33–35]. The exchange correlation functional employed was the Perdew-Burke-Ernzerhof (PBE) functional of generalized gradient approximation. The kinetic energy cutoff of 500 eV was employed. ZnO (002) and WO_3 (001) surface slab models with 24 Zn and 9 W atoms respectively were constructed and the repeating slab was separated by a vacuum spacing of 20 Å. For oxygen-deficient WO_3 , one surface O atoms were removed to model the oxygen vacancy concentration of 7.8%. The calculation for ZnO were performed generalized gradient approximation with the DFT + U. The k -point of static method were set as $4 \times 4 \times 1$ and $3 \times 3 \times 1$. All the structures were optimized until the force on each atom was less than $0.02 \text{ eV}/\text{\AA}$.

3. Results and discussion

3.1. Morphology and crystal structure

As shown in Fig. 2a–c, pure ZnO possesses the highly uniform ZnO nanorod arrays (perpendicular to the FTO surface) with diameter of ca.

400 nm and length of ca. $3.42 \mu\text{m}$, and shows the typical wurtzite hexagonal structure. After the *in-situ* crystallization of WO_3 on ZnO nanorods, the nanorod size became larger and its surface was decorated with a thin coarse layer (Fig. 2d–i). The corresponding EDS spectrum confirmed the existence of W element besides of Zn and O elements (Fig. S1, Supporting Information, SI), suggesting the thin coarse particles wrapping ZnO NA should be tungsten oxide, which forms a ZnO - WO_3 heterojunction structure. With the increase of W precursor (WCl_6) from 5 mg (Zn-W-5) to 15 mg (Zn-W-15) (Fig. 2d–i), the average diameter of the nanorods is increased from ca. 420 nm to 430 nm, and the surface becomes much denser. However, the deposition of WO_3 does not obviously affect the thickness (ca. 3.42 – $3.46 \mu\text{m}$) of ZnO arrays (Fig. 2c,f,i).

XRD patterns of ZnO and $\text{Zn-W-}m$ are shown in Fig. 3a. For pure ZnO NA, the diffraction peaks can be indexed to typical hexagonal wurtzite structure of ZnO (JCPDS No. 36-1451) with an overwhelming diffraction peak located at 34.4° which indicates a preferred orientation of the NAs along c -axis perpendicular to the substrate, and the thin SnO_2 layer on the FTO glass substrate (JCPDS No. 46-1088).

Compared with the strong diffraction signals of ZnO in $\text{Zn-W-}m$, only very trace characteristic peaks located at 65.18° , 68.08° , and 78.61° , referring to hexagonal WO_3 (JCPDS No. 33-1387, Fig. 3b), can be observed. It is worth noting that the loading amount of WO_3 increases slightly with m raised from 1 mg to 15 mg. Moreover, Fig. 3c shows a typical TEM image of ZnO nanorod of Zn-W-5 , and it is obvious to observe the rough surface caused by the coverage of surface WO_3 nanoparticles (NPs). The high-resolution TEM image in Fig. 3d indicates there are many WO_3 NPs in the size of 3–8 nm decorated on ZnO nanorod. From EDS element mapping (Fig. 3e), Zn, W and O elements are dispersed well on the nanorod, suggesting the uniform coverage of WO_3 NPs on ZnO nanorod. The HR-TEM images (Fig. 3d) also confirm the high degree of crystallization of ZnO and WO_3 with clear lattice fringes of 0.260 nm and 0.238 nm, which refer to the interspacing of the (002) planes of the wurtzite ZnO and the (210) planes of the WO_3 , respectively.

3.2. Surface defects and optical properties

X-ray photoelectron spectroscopy (XPS) is then applied to investigate the chemical composition and surface elemental states of as-prepared samples. The survey spectra show the co-existence of Zn, W and O elements in $\text{Zn-W-}m$, confirming the presence of WO_3 in the samples. As shown in Fig. 4a–c, the W4f peak can be divided into four peaks, and the strong peaks at 36.1 and 38.2 eV correspond to W^{6+} , while the weak peaks at 35.2 and 37.5 eV refer to W^{5+} [36]. The presence of W^{5+} signals indicates the existence of oxygen vacancies in WO_3 [27], and the defect amount are similar for all samples (ca. 7.6%), which are caused by the methanol-induced reduction during solvothermal process. As shown in the fitted O1s spectra (Fig. S2a–d, SI), the decoration of WO_3 on ZnO shows three O1s peaks at 532, 531.1 and 529.8 eV, attributed to the physisorbed water, O atoms in the vicinity of surface oxygen vacancies, and lattice oxygen, respectively [37]. Obviously, $\text{Zn-W-}m$ samples show the abundant oxygen vacancies, while no obvious vacancies are observed for pure ZnO . This result is consistent with W4f XPS.

From Fig. 4d, the double peaks at 1043.7 and 1020.1 eV are ascribed to the core levels of $\text{Zn } 2p_{1/2}$ and $\text{Zn } 2p_{3/2}$ of ZnO , respectively. It is worth noting that the loading of WO_{3-x} on the surface of ZnO NA (Zn-W-1 , Zn-W-5 and Zn-W-15) causes obvious high-energy shift of $\text{Zn } 2p$ binding energy, because Zn atoms of $\text{Zn-W-}m$ donate electrons to W atoms due to the lower electronegativity (1.65) than W (2.36). This result confirms the chemical bonding of WO_{3-x} and ZnO via W-O-Zn, which may benefit the interface Z-scheme electron transfer during PEC process.

Moreover, the optical absorption spectra are shown in Fig. 5a, and ZnO NA and WO_{3-x} exhibit steep absorption onset at ca. 395 nm and ca.

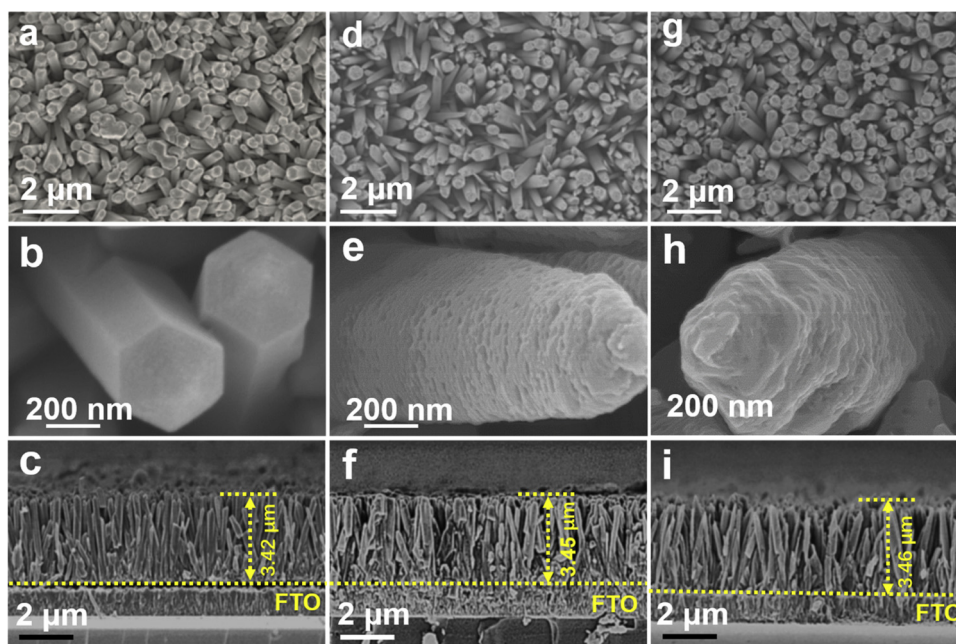


Fig. 2. Top-view and cross-sectional-view SEM images of pure ZnO (a-c); Zn-W-5 (d-f) and Zn-W-15 (g-i).

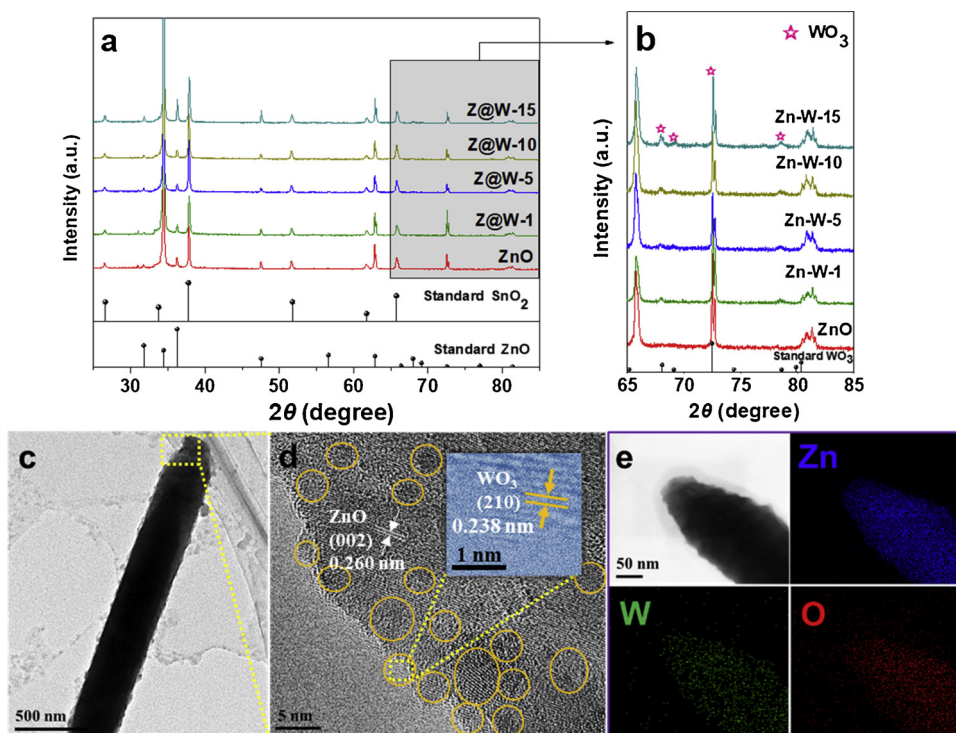


Fig. 3. X-ray diffraction (XRD) patterns of ZnO and Zn-W-*m* (a,b). TEM (c,d) and EDS mapping images (e) of Zn-W-5.

459 nm, respectively. Specially, a slightly increased absorption at 400–800 nm is observed for Zn-W-*m*, which should be related to the decoration of WO_{3-x}. Meanwhile, the obvious enhanced absorption at ca. 600 nm for pure WO_{3-x} is caused by the unique oxygen-defect structure of WO_{3-x} [24,38–40], and the similar results are observed for Zn-W-*m* samples.

Since the efficient separation of photoinduced charges is vital for highly photocatalytic or PEC activity [41], the steady-state photoluminescence (PL) spectra of the samples were conducted and shown in Fig. 5b. All samples show a strong PL emission signal at 370–380 nm, which is the typical radiative band-to-band emission of ZnO, but the

peak intensity for the samples are different. Notably, Zn-W-*m* exhibits much lower PL intensity than ZnO NA, suggesting the former possesses higher efficiency in charge separation than the latter. Meanwhile, the fluorescence lifetime of charge carriers and quantum yield (QY) were measured (Fig. 5c, Table S1, SI). It is worth noting that the average fluorescence lifetimes of Zn-W-*m* were longer than ZnO NA (6.07 ns), and the QYs of Zn-W-*m* were higher than ZnO NA (8.24%), which means the construction of Z-scheme structure can accelerate the charge transfer process [42,43]. Among Zn-W-*m*, the most effective charge separation is observed for Zn-W-5, with fluorescence lifetime of 11.68 ns and QY of 18.30%.

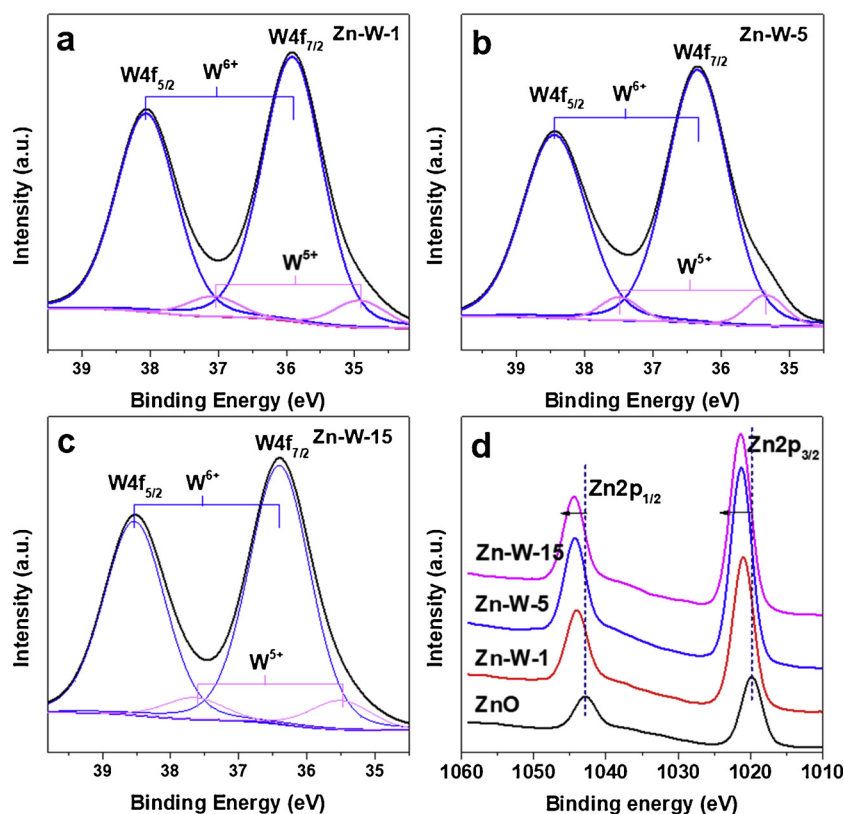


Fig. 4. W4f (a–c) and Zn2p (d) XPS spectra of Zn-W-*m* and pure ZnO NA.

3.3. Photoelectrochemical (PEC) water splitting

PEC catalysis is emerging as one of the promising methods for solar hydrogen and oxygen generation, and has attracted increasing interest. Therefore, the as-prepared Zn-W-*m* samples were applied for PEC water splitting. As shown in Fig. 6a (*J-V* curves), the samples show no current in dark. But under light illumination (100 mW/cm^2), ZnO NA shows an on-set potential of 0.41 V vs. RHE and a photocurrent of 1.12 mA/cm^2 at the potential of 1.23 V vs. RHE. After WO_{3-x} loading, Zn-W-*m* samples perform much better than ZnO NA, and their PEC activities first increase with *m* rising from 1 to 5, and then decrease when further increasing *m* up to 15. Notably, Zn-W-5 photoanode shows the lowest on-set potential of 0.36 V vs. RHE, and the best photocurrent density of 2.39 mA/cm^2 at 1.23 V vs. RHE, which is 2.13 times higher than ZnO NA.

Then, the incident-photon-to-current-conversion efficiency (IPCE) tests of Zn-W-*m* and ZnO were performed and shown in Fig. 6b. The wavelength of the initial light response of samples are all below ca.

400 nm (which is almost the band gap of ZnO), and the IPCE increases gradually when reducing the irradiation-light wavelength. Among the samples, Zn-W-5 shows much higher IPCE than others, with its value up to 84% (at 370 nm). The activity trend from IPCE is Zn-W-5 > Zn-W-1 > Zn-W-10 > Zn-W-15 > ZnO NA, the same trend with PEC current (*J-V* curves). Meanwhile, the applied bias photon-to-current efficiency (ABPE) plots of photoanodes are shown in Fig. 6c, and the maximum ABPE of ZnO NA only reaches 0.326%, while the decoration of WO_{3-x} on ZnO NA significantly increases ABPE value and leads to the left shift of the peak position. And the maximum ABPE values for Zn-W-1, Zn-W-5, Zn-W-10 and Zn-W-15 are 0.693%, 0.735%, 0.623% and 0.535% at applied bias of 0.798, 0.779, 0.801, 0.805 V vs. RHE, respectively. Among them, Zn-W-5 exhibits the highest ABPE value, which is 2.25 times higher than that of ZnO NA.

Moreover, in electrochemical impedance spectra (EIS), the arc radius of Nyquist plots can be used to evaluate the charge transfer resistance at the semiconductor/electrolyte interface, and smaller arc radius implies smaller charge transfer resistance [44]. From EIS plots at

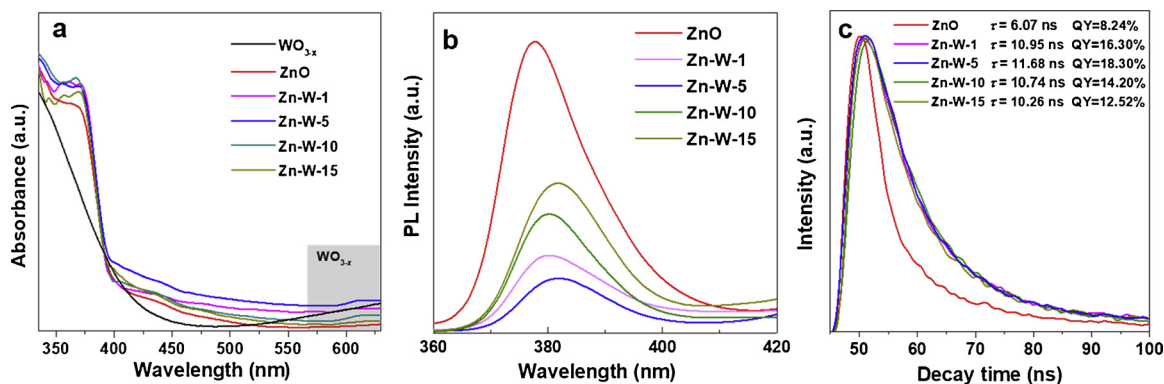


Fig. 5. (a) UV-vis DRS of ZnO, WO_{3-x} and Zn-W-*m*, (b) steady-state PL spectra and (c) Time-resolved PL decay spectra of ZnO and Zn-W-*m*.

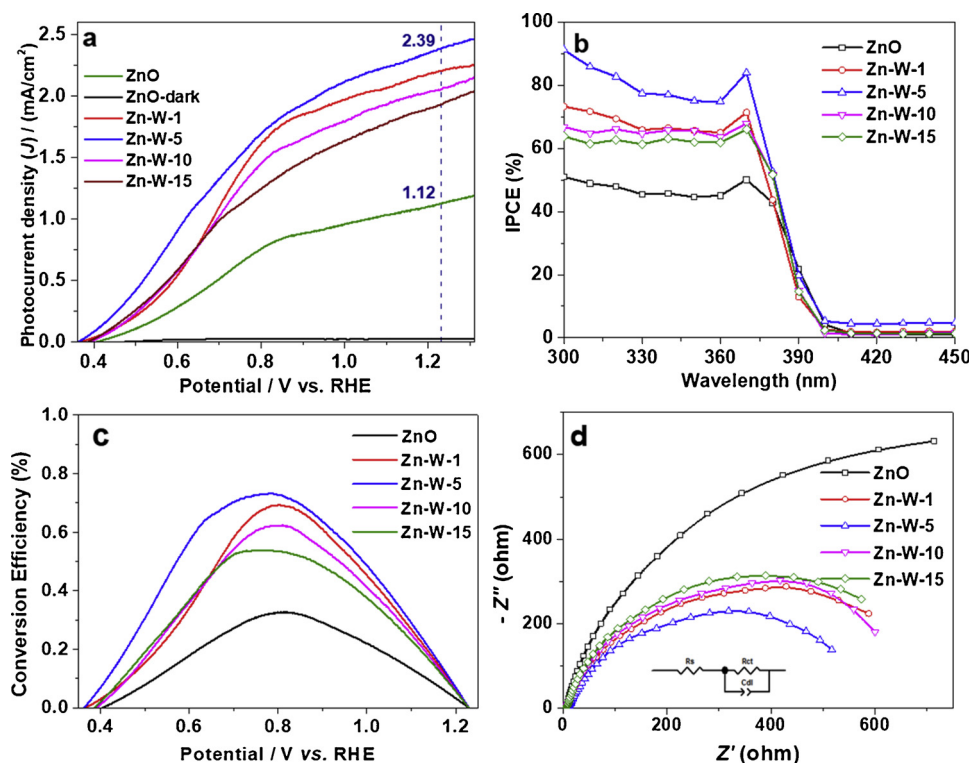


Fig. 6. (a) *J*-*V* curves, (b) IPCE, (c) ABPE and (d) electrochemical impedance spectra (EIS) of ZnO NA and Zn-W-*m*.

1.0 V vs. RHE (Fig. 6d), the charge transfer resistance of the samples was calculated based on fitting model (see the inset in Fig. 6d). The charge transfer resistance (R_{ct}) is in the order of $R_{ct}(\text{ZnO NA}, 5082 \Omega) > R_{ct}(\text{Zn-W-15}, 1929 \Omega) > R_{ct}(\text{Zn-W-10}, 1299 \Omega) > R_{ct}(\text{Zn-W-1}, 1177 \Omega) > R_{ct}(\text{Zn-W-5}, 1070 \Omega)$. It is obvious that the decoration of WO_{3-x} NPs on ZnO NA can improve the conductivity under light irradiation, which will make electrons rapidly transferring and reduce the recombination of photoexcited holes and electrons. Specifically, with the optimal WO_{3-x} loading, Zn-W-5 shows the highest conductivity and further the PEC performance. In addition, the produced H_2 and O_2 were measured with a gas chromatograph (Fig. S3, SI) [45]. The practical volumes of H_2 and O_2 evolution are close to their theoretical values (at 1.1 V vs. RHE), and the H_2 volume is nearly twice of O_2 volume, which means the photocurrent of Zn-W-5 photoanode is caused by the water oxidation. Besides, Zn-W-5 also exhibits high PEC stability with a very steady photocurrent (Fig. S4, SI).

3.4. Z-scheme-mediated PEC mechanism

The above results confirm that the structure of ZnO- WO_{3-x} shows higher charge-separation efficiency than ZnO NA. However, what is the real function of surface WO_{3-x} (It is worth noting that it will decrease the PEC activity if the typical II heterojunction forms)?

Generally, the charge transfer between two semiconductors depends on the interface band bending, which is further determined by their band structures and Fermi levels. When two semiconductors are in direct contact, the band edges in the semiconductor with high Fermi level will bend upward continuously toward the interface, and those with low Fermi level will bend downward [20,46–48]. The downward band bending allows the electrons flow out freely but inhibits the holes, and *vice versa*. From UV-vis DRS (Fig. S5, SI), the band gaps of ZnO and WO_{3-x} are calculated to be 3.12 and 2.70 eV, respectively. As shown in Fig. S2e (SI), the valence band (VB) edges tested by XPS are 2.92 and 3.50 eV for ZnO and WO_{3-x} , respectively, consistent with previous reports [22,23]. The density functional theory (DFT) calculations of work function (W_F , Fig. 7a,b) were performed, and the ΔE_F by subtracting

$W_F(\text{defected } \text{WO}_3)$ with $W_F(\text{ZnO})$ is +0.48 eV, indicating the Z-scheme charge-transfer direction in the heterojunction of ZnO- WO_{3-x} [48]. Therefore, when they contact directly with each other, the band edge in ZnO will bend upward while that in WO_3 will bend downward towards the interface (Fig. 7c), with the recombination of the holes from ZnO and electrons from defected WO_3 . Meanwhile, the electrons in ZnO will rapidly move to the counter electrode (Pt) via the external circuit for further hydrogen generation, while the accumulated hole in surface defected WO_3 will participate the water oxidation reaction to produce oxygen. In addition, the introduction of oxygen vacancies to WO_3 can form quasi-continuous energy levels between VB and CB, which induce the formation of ohmic contact and lower the interfacial electric resistance [27].

To further confirm the Z-scheme charge transfer, the photodeposition of PbO_2 was carried out. As revealed in Fig. 7d, PbO_2 NPs (with lattice fringe of 0.25 nm) are selectively photodeposited on the surface of WO_{3-x} (with lattice fringe of 0.238 nm), indicating the photoinduced holes should be trapped on WO_{3-x} of Zn-W-5 during light irradiation, further confirming the direct Z-scheme heterojunction structure.

3.5. Piezoelectric-photoelectrochemical (PE-PEC) water splitting

It is worth noting that ZnO is an important piezoelectric (PE) material because the hexagonal ZnO NA possesses the anisotropic property between the *c*-axis direction and the perpendicular *c*-axis direction [49]. Therefore, the introduction of PE polarization in Zn-W-*m* generated by the bending of nanorod arrays may significantly tune and enhance the Z-scheme structure, and further increase the PEC performance. Here, the water flow induced by stirring the electrolyte was applied to generate the piezoelectric field of the Z-scheme photoanode (Zn-W-5), and the stirring rate (0–1000 rpm) was tuned to enhance this effect.

As the above *J*-*V* curves (Fig. 6a) show, Zn-W-5 shows an on-set potential of 0.36 V vs. RHE and a photocurrent of 2.39 mA/cm² at 1.23 V vs. RHE under light illumination. Importantly, the 300 rpm stirring (PE polarization) can significantly decrease the on-set potential

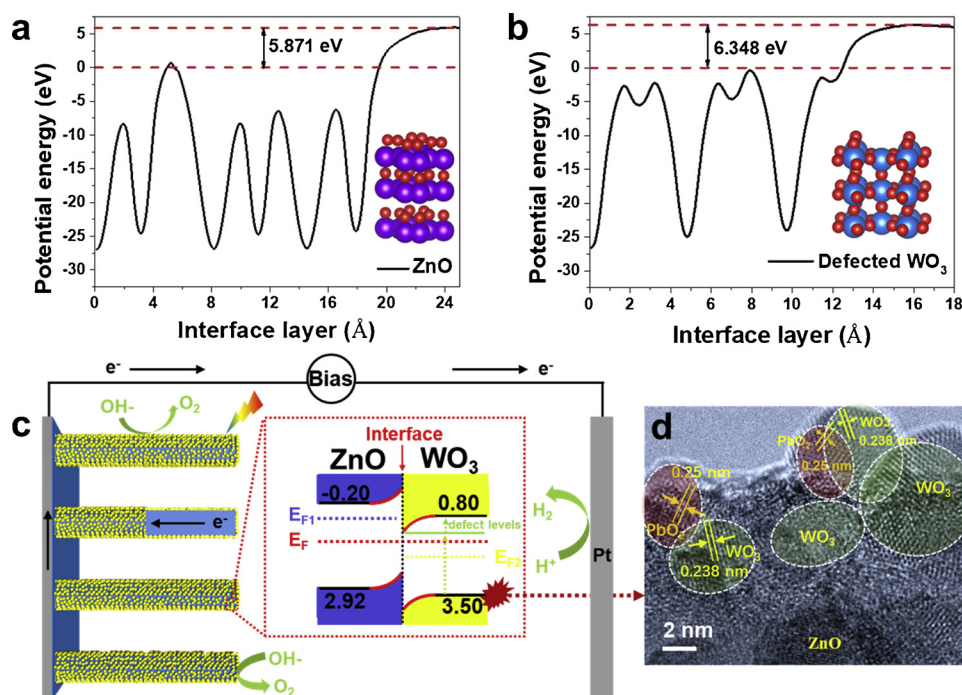


Fig. 7. DFT calculated potential diagrams of ZnO (a) and WO_{3-x} (b). (c) Schematic charge-transfer process in Zn-W-m and (d) HR-TEM image of Zn-W-5 photo-deposited with PbO_2 .

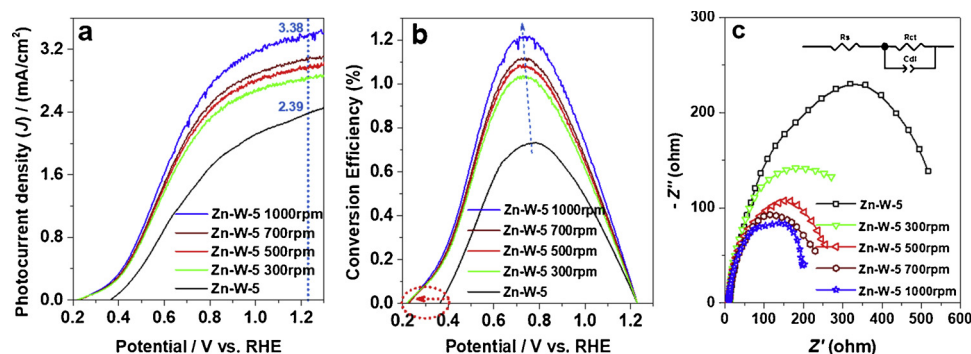


Fig. 8. (a) J-V curves, (b) ABPE, and (c) EIS spectra of Zn-W-5 at different stirring rates.

to 0.23 V vs. RHE and increase the photocurrent to 3.09 mA/cm^2 at 1.23 V vs. RHE (Zn-W-5-300 rpm, Fig. 8a). And the PE-PEC activity increases with the stirring rate rising from 300 rpm to 1000 rpm. Especially, under 1000 rpm, Zn-W-5 shows a PE-PEC photocurrent of 3.38 mA/cm^2 at 1.23 V vs. RHE, which is 1.41 times higher than Zn-W-5 without stirring, and 3.02 times higher than pure ZnO NA. Similarly, from Fig. 8b, the maximum ABPE of Zn-W-5 increases and the on-set potential have apparently left shift (from 0.36 V to 0.21 V vs. RHE) with the stirring rate rising from 300 rpm to 1000 rpm, which should attribute to the enhancement of PE polarization inside ZnO NA. As shown in EIS (Fig. 8c), the charge-transfer resistance (R_{ct}) of Zn-W-5 can be decreased significantly by the PE polarization. For example, $R_{ct}(\text{Zn-W-5}) = 1070 \Omega$, while $R_{ct}(\text{Zn-W-5-500 rpm}) = 280 \Omega$, and $R_{ct}(\text{Zn-W-5-1000 rpm}) = 221.7 \Omega$, confirming the accelerated charge-transfer process by the PE polarization. In addition, Zn-W-5-1000 rpm shows a relatively high stability, with the oxygen defects unchanged (Fig. S6, SI).

The above results confirm the important role of PE polarization on promoting the PEC water splitting performance of Z-scheme photoanodes. However, the PEC enhancement can be also realized by the improvement of mass transfer during the stirring. Therefore, the controlled trials were conducted to exclude other contributions.

(1) The blank tests. The PEC results show that there are no dark

current densities for ZnO and Zn-W-5 with or without stirring (Fig. S7, SI), indicating the light irradiation is the key activation for PEC and the piezoelectric current can be ignored.

(2) The comparison between Zn-W-5, ZnO and TiO_2 nanorod arrays (NA). As shown in Fig. 9, the application of stirring in PEC cell can obviously improve the PEC activity of Zn-W-5 and ZnO NA, which increases with the rise of stirring rate, but it has no effects on TiO_2 NA (even under high stirring rate of 1000 rpm). Since TiO_2 , ZnO and Zn-W-5 NA have the similar nanorod morphologies (Fig. 2, Fig. S8, SI), the above result indicates the enhancement of mass transfer by stirring can be ignored, and the stirring-rate-dependent PEC activity should be related to the PE effect of ZnO (because TiO_2 has no PE effect). Importantly, the PE enhancement is more obvious for Zn-W-5 than ZnO NA, confirming the PE polarization could tune the interface band structure for more effective Z-scheme charge transfer.

(3) The comparison of solution flow directions. To further confirm the PE effect on PEC performances, we tuned the located place of the tested photoanodes and realize the vertical solution flow and parallel solution flow of nanorod arrays (Fig. 9). Obviously, the parallel solution flow of NA (Zn-W-5-P and ZnO-P) shows no effects on PEC performance. The PEC performance comparison between two kinds of solution flow directions indicates the bending of NA shows much more PE

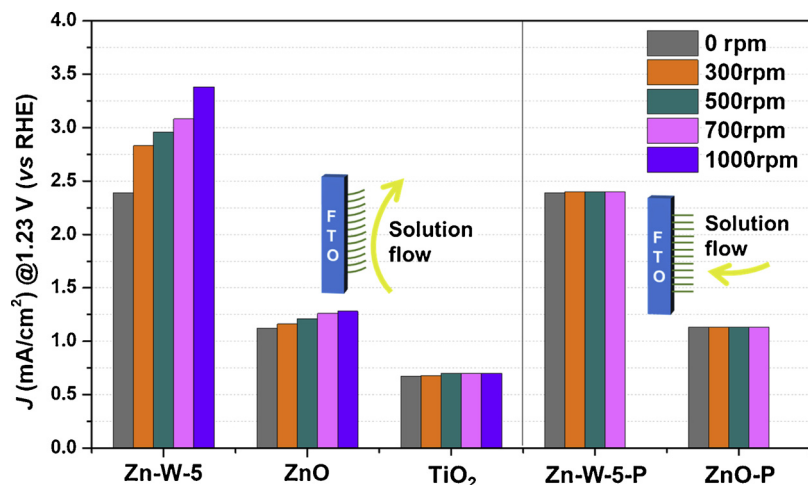


Fig. 9. The photocurrents (at 1.23 V vs. RHE) of the samples under different stirring rates and solution flow directions (Fig. S9, SI). The ZnO and TiO₂ are in the morphology of nanorod arrays (Fig. 2, Fig. S8, SI). The flow directions are two types: the vertical flow of nanorod arrays (for Zn-W-5, ZnO and TiO₂), and the parallel flow of nanorod arrays (for Zn-W-5-P and ZnO-P).

effect than the pressure on NA top.

Base on the above results, the PE-polarized Z-scheme process has been deduced. During the solution stirring (the vertical flow of NAs), the nanorod will bend aside and a piezoelectric field can be created by crossing ZnO with negative piezopotential on the compressive strain region and positive piezopotential on the tensile strain region [50,51], owing to the dipole moment generated by applying stress at the apex of the structure [52] (Fig. 10a). Therefore for pure ZnO NA, the piezopotential inside the nanorods can drive the photogenerated electrons/holes to migrate along opposite directions, avoiding charge recombination [53], and further enhance the PEC performance. Differently for Zn-W-*m* (with Z-scheme charge transfer), the piezopotential inside the composite structures can not only promote the separation and transportation of photogenerated charges, but also change the interface electronic structure significantly between WO_{3-x} and ZnO NAs. Especially on the tensile strain region, the accumulated electrons by positive piezopotential promotes the Fermi level to move toward to CB of ZnO, which will significantly enhance the formed Z-scheme charge transfer (with charge recombination from WO_{3-x} CB band and ZnO VB band) between ZnO and WO_{3-x} (Fig. 10b). Therefore, the PE-polarized Z-scheme ZnO-WO_{3-x} heterojunction realized much higher Z-scheme efficiently, and increasing the stirring rate can enhance this effect and further the PEC performance (Fig. 9).

4. Conclusion

With the suitable band structures and Fermi levels, the direct Z-scheme ZnO-WO_{3-x} nanorod arrays for PE-PEC water splitting were constructed by *in-situ* solvothermal treatment. The decorated WO_{3-x} nanoparticles were tuned to optimize the morphology and optical absorption, and the obtained sample Zn-W-5 shows the best PEC performance, with the lowest on-set potential of 0.36 V vs. RHE, and the best photocurrent density of 2.39 mA/cm² at 1.23 V vs. RHE. Furthermore, the introduction of stirring treatment leads to obvious piezoelectric polarization for ZnO NA, which tunes the Fermi level and significantly enhances the Z-scheme effect (and increasing stirring rate can gradually enhance the PE effect). Meanwhile, the PE polarized Z-scheme Zn-W-5 shows much higher PEC activity (with the stirring rate of 1000 rpm), with the photocurrent at 3.38 mA/cm² at 1.23 V vs. RHE, which is 3.02 times higher than pure ZnO NA. This work provides a facile and effective approach to construct the direct Z-scheme heterojunction and discovers the piezoelectric effect for the enhancement of Z-scheme charges-transfer process.

Declaration of Competing Interest

The authors declare that they have no known competing financial interests or personal relationships that could have appeared to influence the work reported in this paper.

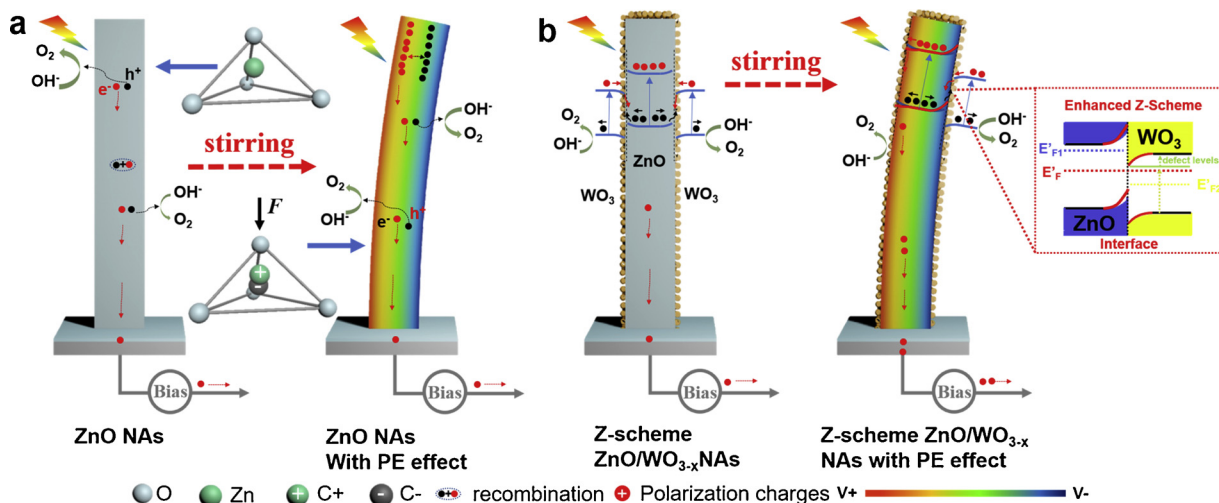


Fig. 10. (a) Schematic illustration of polarization process of ZnO, (b) the PE-PEC process and the energy band diagram of Zn-W-*m*.

Acknowledgements

The authors appreciate the supports from the National Natural Science Foundation of China (21506156, U1462119, 21676193) and the Tianjin Municipal Natural Science Foundation (16JCQNJC05200, 15JCZDJC37300).

Appendix A. Supplementary data

Supplementary material related to this article can be found, in the online version, at doi:<https://doi.org/10.1016/j.apcatb.2019.118079>.

References

- [1] K. Ma, O. Yehezkeili, D.W. Domaille, H.H. Funke, J.N. Cha, *Angew. Chem Int. Ed.* 54 (2015) 11490–11494.
- [2] A. Iwase, S. Yoshino, T. Takayama, Y.H. Ng, R. Amal, A. Kudo, *J. Am. Chem. Soc.* 138 (2016) 10260–10264.
- [3] Z. Pan, T. Hisatomi, Q. Wang, S. Chen, M. Nakabayashi, N. Shibata, C. Pan, T. Takata, M. Katayama, T. Minegishi, A. Kudo, *K. Domen, ACS Catal.* 6 (2016) 7188–7196.
- [4] P. Zhou, J. Yu, M. Jaroniec, *Adv. Mater.* 26 (2014) 4920–4935.
- [5] H. Tada, T. Mitsui, T. Kiyonaga, T. Akita, K. Tanaka, *Nat. Mater.* 5 (2006) 782–786.
- [6] T. Hisatomi, J. Kubota, K. Domen, *Chem. Soc. Rev.* 43 (2014) 7520–7535.
- [7] Y.-P. Yuan, L.-W. Ruan, J. Barber, S.C. Joachim Loo, C. Xue, *Energy Environ. Sci.* 7 (2014) 3934–3951.
- [8] A.P. Singh, N. Kodan, B.R. Mehta, A. Held, L. Mayrhofer, M. Moseler, *ACS Catal.* 6 (2016) 5311–5318.
- [9] Z. Li, W. Luo, M. Zhang, J. Feng, Z. Zou, *Energy Environ. Sci.* 6 (2013) 347–370.
- [10] B. Ma, J. Kim, T. Wang, J. Li, K. Lin, W. Liu, S. Woo, *RSC Adv.* 5 (2015) 79815–79819.
- [11] I. Gonzalez-Valls, M. Lira-Cantu, *Energy Environ. Sci.* 2 (2009) 19–34.
- [12] C. Xu, Z.L. Wang, *Adv. Mater.* 23 (2011) 873–877.
- [13] Q. Zhang, C.S. Dandaneau, X. Zhou, G. Cao, *Adv. Mater.* 21 (2009) 4087–4108.
- [14] Y. Qiu, K. Yan, H. Deng, S. Yang, *Nano Lett.* 12 (2012) 407–413.
- [15] J.M. Li, H.Y. Cheng, Y.H. Chiu, Y.J. Hsu, *Nanoscale* 8 (2016) 15720–15729.
- [16] Y.-C. Pu, W.-H. Lin, Y.-J. Hsu, *Appl. Catal. B: Environ.* 163 (2015) 343–351.
- [17] R. Li, F. Zhang, D. Wang, J. Yang, M. Li, J. Zhu, X. Zhou, H. Han, C. Li, *Nat. Commun.* 4 (2013) 1432.
- [18] B. Ma, X. Wang, K. Lin, J. Li, Y. Liu, H. Zhan, W. Liu, *Int. J. Hydrogen Energy* 42 (2017) 18977–18984.
- [19] B.J. Ma, J.S. Kim, C.H. Choi, S.I. Woo, *Int. J. Hydrogen Energy* 38 (2013) 3582–3587.
- [20] L.J. Zhang, S. Li, B.K. Liu, D.J. Wang, T.F. Xie, *ACS Catal.* 4 (2014) 3724–3729.
- [21] Y. Xu, M.A.A. Schoonen, *Am. Mineral.* 85 (2000) 543–556.
- [22] J. Hu, L. Wang, P. Zhang, C. Liang, G. Shao, *J. Power Sources* 328 (2016) 28–36.
- [23] S. Bao, Q. Wu, S. Chang, B. Tian, J. Zhang, *Catal. Sci. Technol.* 7 (2017) 124–132.
- [24] Z.F. Huang, J. Song, L. Pan, X. Zhang, L. Wang, J.J. Zou, *Adv. Mater.* 27 (2015) 5309–5327.
- [25] K. Manthiram, A.P. Alivisatos, *J. Am. Chem. Soc.* 134 (2012) 3995–3998.
- [26] H. Zheng, J.Z. Ou, M.S. Strano, R.B. Kaner, A. Mitchell, K. Kalantar-zadeh, *Adv. Funct. Mater.* 21 (2011) 2175–2196.
- [27] X. Jia, M. Tahir, L. Pan, Z.-F. Huang, X. Zhang, L. Wang, J.-J. Zou, *Appl. Catal. B: Environ.* 198 (2016) 154–161.
- [28] L. Pan, S. Wang, J. Xie, L. Wang, X. Zhang, J.-J. Zou, *Nano Energy* 28 (2016) 296–303.
- [29] W. Zhao, Y. Liu, Z. Wei, S. Yang, H. He, C. Sun, *Appl. Catal. B: Environ.* 185 (2016) 242–252.
- [30] S.J.A. Moniz, J. Zhu, J. Tang, *Adv. Energy Mater.* 4 (2014) 1301590.
- [31] X. Zhang, Y. Liu, Z. Kang, *ACS Appl. Mater. Interfaces* 6 (2014) 4480–4489.
- [32] R. Li, H. Han, F. Zhang, D. Wang, C. Li, *Energy Environ. Sci.* 7 (2014) 1369–1376.
- [33] S. Holdren, R. Tsyshkevsky, K. Fears, J. Owrutsky, T. Wu, X. Wang, B.W. Eichhorn, M.M. Kukulja, M.R. Zachariah, *ACS Catal.* 9 (2018) 902–911.
- [34] E. Albanese, C. Di Valentin, G. Pacchioni, *ACS Appl. Mater. Interfaces* 9 (2017) 23212–23221.
- [35] C. Zhang, M. Shao, F. Ning, S. Xu, Z. Li, M. Wei, D.G. Evans, X. Duan, *Nano Energy* 12 (2015) 231–239.
- [36] C. Han, Z. Chen, N. Zhang, J.C. Colmenares, Y.-J. Xu, *Adv. Funct. Mater.* 25 (2015) 221–229.
- [37] Z. Sun, R. Huo, C. Choi, S. Hong, T.-S. Wu, J. Qiu, C. Yan, Z. Han, Y. Liu, Y.-L. Soo, Y. Jung, *Nano Energy* 62 (2019) 869–875.
- [38] R. Wu, J. Zhang, Y. Shi, D. Liu, B. Zhang, *J. Am. Chem. Soc.* 137 (2015) 6983–6986.
- [39] G. Xi, S. Ouyang, P. Li, J. Ye, Q. Ma, N. Su, H. Bai, C. Wang, *Angew. Chem. Int. Ed.* 51 (2012) 2395–2399.
- [40] J. Song, Z.-F. Huang, L. Pan, J.-J. Zou, X. Zhang, L. Wang, *ACS Catal.* 5 (2015) 6594–6599.
- [41] L. Pan, S. Wang, W. Mi, J. Song, J.-J. Zou, L. Wang, X. Zhang, *Nano Energy* 9 (2014) 71–79.
- [42] Y.P. Xie, Y. Yang, G. Wang, G. Liu, *J. Colloid Interface Sci.* 503 (2017) 198–204.
- [43] C. Li, Z. Zhang, C. Han, Z. Hu, X. Tang, J. Du, Y. Leng, K. Sun, *Nano Energy* 40 (2017) 195–202.
- [44] S. Wang, L. Pan, J.J. Song, W. Mi, J.J. Zou, L. Wang, X. Zhang, *J. Am. Chem. Soc.* 137 (2015) 2975–2983.
- [45] J. Qi, D. Kong, D. Liu, L. Pan, Y. Chen, X. Zhang, J.-J. Zou, *RSC Adv.* 9 (2019) 15629–15634.
- [46] Z. Zhang, J.T. Yates Jr., *Chem. Rev.* 112 (2012) 5520–5551.
- [47] S. Bai, X. Li, Q. Kong, R. Long, C. Wang, J. Jiang, Y. Xiong, *Adv. Mater.* 27 (2015) 3444–3452.
- [48] Z.-F. Huang, J. Song, X. Wang, L. Pan, K. Li, X. Zhang, L. Wang, J.-J. Zou, *Nano Energy* (2017).
- [49] L. Dong, S. Niu, C. Pan, R. Yu, Y. Zhang, Z.L. Wang, *Adv. Mater.* 24 (2012) 5470–5475.
- [50] Z.L. Wang, J. Song, *Science* 312 (2006) 242–246.
- [51] Z.L. Wang, *Nano Today* 5 (2010) 540–552.
- [52] Z.L. Wang, *Adv. Mater.* 24 (2012) 4632–4646.
- [53] Q. Yang, Y. Liu, C. Pan, J. Chen, X. Wen, Z.L. Wang, *Nano Lett.* 13 (2013) 607–613.